Evaluating the impacts of cloud processing on resuspended aerosol particles after cloud evaporation using a particle-resolved model

Yu YAO[1], Matthew L. Dawson[2], Donald Dabdub[3], and Nicole Riemer[1]

[1]University of Illinois at Urbana Champaign
[2]National Center for Atmospheric Research
[3]University of California, Irvine

November 24, 2022

Abstract

Aerosol particles undergo physical and chemical changes during cloud processes. In this work, we quantified the changes in aerosol mixing state using a particle-resolved model. To this end, we coupled the particle-resolved aerosol model PartMC-MOSAIC with the aqueous chemistry module CAPRAM 2.4 and designed cloud parcel simulations that mimicked several cloud cycles that a particle population may be exposed to in an urban environment. Aqueous-phase chemistry during these cloud cycles affected aerosol mixing state and the particles' potential to act as cloud condensation nuclei (CCN) significantly, with the largest differences after the first cloud cycle. The mean size and total dry mass of the population increased by 24% and 219%, respectively, after the first cycle, while the increments were only 5% and 38% after the fourth cycle. The formation of ammonium sulfate and nitrate were responsible for those changes. Cloud processing increased the internally mixed state of all particle populations, with the mixing state index increasing from 50 to 83 percentage points after four cloud cycles. The CCN concentrations for supersaturations lower than 0.23% increased. For example, for supersaturation levels of 0.02%, the CCN concentration increased from 25 to 547 cm^{-3}. Brownian coagulation led to an increase of the CCN/CN ratio for supersaturation levels higher than 0.2%. The ratio increased by 4.1% at the supersaturation level 0.5%. Total number concentration and CCN concentration decreased by 5.9% and 1.7%, respectively, when Brownian coagulation is considered. These findings highlight the complex influence of cloud processing on particle properties.

Evaluating the impacts of cloud processing on resuspended aerosol particles after cloud evaporation using a particle-resolved model

Yu Yao[1], Matthew L. Dawson[2,3], Donald Dabdub[3], Nicole Riemer[1]

[1]Department of Atmospheric Sciences, University of Illinois at Urbana-Champaign, Urbana, Illinois, USA
[2]National Center for Atmospheric Research, Boulder, Colorado, USA
[3]Department of Mechanical and Aerospace Engineering, University of California, Irvine, CA, USA

Key Points:

- Aqueous-phase chemistry processes cause aerosol populations to be more internally mixed.
- CCN concentration increases substantially after cloud processing for supersaturations lower than the maximum cloud supersaturation.
- Coagulation within clouds has a negligible impact on aerosol mixing state.

Corresponding author: Nicole Riemer, nriemer@illinois.edu

Abstract

Aerosol particles undergo physical and chemical changes during cloud processes. In this work, we quantified the changes in aerosol mixing state using a particle-resolved model. To this end, we coupled the particle-resolved aerosol model PartMC-MOSAIC with the aqueous chemistry module CAPRAM 2.4 and designed cloud parcel simulations that mimicked several cloud cycles that a particle population may be exposed to in an urban environment. Aqueous-phase chemistry during these cloud cycles affected aerosol mixing state and the particles' potential to act as cloud condensation nuclei (CCN) significantly, with the largest differences after the first cloud cycle. The mean size and total dry mass of the population increased by 24% and 219%, respectively, after the first cycle, while the increments were only 5% and 38% after the fourth cycle. The formation of ammonium sulfate and nitrate were responsible for those changes. Cloud processing increased the internally mixed state of all particle populations, with the mixing state index χ increasing from 50 to 83 percentage points after four cloud cycles. The CCN concentrations for supersaturations lower than 0.23% increased. For example, for supersaturation levels of 0.02%, the CCN concentration increased from 25 to 547 cm^{-3}. Brownian coagulation led to an increase of the CCN/CN ratio for supersaturation levels higher than 0.2%. The ratio increased by 4.1% at the supersaturation level 0.5%. Total number concentration and CCN concentration decreased by 5.9% and 1.7%, respectively, when Brownian coagulation is considered. These findings highlight the complex influence of cloud processing on particle properties.

Plain Language Summary

Every cloud droplet contains at least one aerosol nucleus. The composition and mass of this nucleus can be changed during a cloud's lifetime by several chemical and physical processes. Once the cloud evaporates, a modified aerosol population is released into the atmosphere compared to the population that formed the cloud, which may also have different impacts on climate. In this work, we used a particle-resolved process model to study the effects of cloud processing on aerosols within clouds. This modeling approach is suitable for this research because each particle is tracked individually, which allows us to quantify changes in particle composition without simplifying assumptions, such as averaging composition within predescribed size ranges. Because of the formation of ammonium sulfate and nitrate in the cloud, particles that formed cloud droplets grew larger and were more likely to form cloud droplets in future cloud cycles. Overall, cloud processing by aqueous-phase chemistry produced aerosol populations where the particles look more similar to each other in composition.

1 Introduction

Atmospheric aerosol particles are complex mixtures of different chemical species reflecting the fact that they originate from different emission sources and experience various aging processes in the atmosphere (Riemer et al., 2009; Li et al., 2011; Bondy et al., 2018; Healy et al., 2014; Rissler et al., 2014). Aging processes include processes in the cloud-free atmosphere such as coagulation, heterogeneous reactions on the particles' surface, and the formation of coatings from organic and inorganic secondary aerosol. They also include processes in clouds (Lance et al., 2017) such as aqueous-phase chemistry within cloud droplets forming inorganic and organic aerosol material, and collision-coalescence of particles and droplets within a cloud. When clouds evaporate, aerosol populations are released into the atmosphere with modified properties compared to the populations that formed the cloud. This, in turn, changes the aerosols' impacts on clouds in the next cloud cycle (Hoose et al., 2008), and therefore this process is important for 3D chemical transport models to include. At the same time it poses challenges to be represented in these models (Gao et al., 2016).

Specifically, in-cloud processes have been shown to result in the observed doubly peaked size distributions since material from the gas phase and from smaller particles is transferred to the accumulation mode size range (Hoppel et al., 1986; Noble & Hudson, 2019). It has also been observed that cloud droplets of different sizes may differ in their acidity (Collett et al., 1994; Pye et al., 2020). This has important implications for the rates of aqueous-phase sulfate formation (Hoag et al., 1999), which may depend on pH, and this needs to be considered when representing these processes in cloud microphysics models (Hegg & Larson, 1990; Barth, 2006). Because of the non-linearity of aqueous chemistry processes, models predict larger rates of sulfate formation when using a more realistic size-resolved droplet representation compared to using a prescribed single droplet size.

In this study, we not only considered the variation of aerosol (and cloud droplet) composition with size, but also the variation of composition within a narrow size range, commonly referred to as mixing state (Winkler, 1973; Riemer et al., 2019). Our goal in this study was to quantify the changes in aerosol mixing state due to in-cloud aqueous-phase chemistry and coagulation processes. Aerosol mixing state impacts the aerosols' effects on health (Ching & Kajino, 2018), their absorption and scattering of sunlight (Lesins et al., 2002; Fierce et al., 2020), and their ability to act as cloud condensation and ice nuclei (Broekhuizen et al., 2006; Bhattu & Tripathi, 2015; Knopf et al., 2018).

Mixing state is, on the one hand, a factor in determining which particles activate and form cloud droplets, thereby determining cloud properties (Ching et al., 2012, 2016). On the other hand, mixing state can be modified by in-cloud processes. For example, observations using online single-particle mass spectrometry during the HCCT-2010 field campaign showed that cloud residuals contain more sulfate and nitrate compared to the below-cloud aerosol (Roth et al., 2016), resulting in a change of aerosol mixing state.

Model simulations of aerosol mixing state are challenging, and particularly rare when it comes to simulating in-cloud processes. Regional or global models use simplified assumptions about aerosol activation and aerosol mass and size changes due to cloud processing, which are determined by the underlying model representation of aerosol and cloud droplets. For example, in the CMAQ model, which uses a modal aerosol representation, the sulfate mass produced by in-cloud chemistry is added to the entire accumulation mode (Ervens, 2015; Fahey et al., 2017). High-resolution cloud models typically use a size-resolved fixed-bin microphysical model (Flossmann, 1994; Feingold et al., 1996) and resolve aerosol particles and cloud droplets by separate distributions, thus internally mixing all same-sized particles or droplets. Similarly, accurate parcel models most frequently use a size-resolved moving-bin approach (Kreidenweis et al., 2003; Cooper et al., 1997), again losing aerosol history and composition information within each size bin. To preserve some composition information, 2D aerosol models have been used, resolving cloud droplet size and aerosol dry volume (Bott et al., 1996; Ovchinnikov & Easter, 2010). However, increasing the dimension beyond 2D to treat composition variation of the aerosol in more detail would be computationally prohibitively expensive. Lagrangian cloud microphysics models have also been developed that can track information on a droplet level (Shima et al., 2009; Andrejczuk et al., 2008; Grabowski et al., 2019; Sölch & Kärcher, 2010; Unterstrasser & Sölch, 2014; Jaruga & Pawlowska, 2018). However, their focus has been the study of cloud microphysics rather than the modification of aerosol composition. While Jaruga and Pawlowska (2018) consider some aqueous-phase chemistry processes, their representation of the aerosol is comparatively simple and questions about mixing state have not yet been addressed.

For our study, we used the aerosol model PartMC-MOSAIC (Particle Monte Carlo-Model for Simulating Aerosol Interactions and Chemistry) (Riemer et al., 2009; Zaveri et al., 2008) as aerosol and cloud parcel model. This stochastic particle-resolved model explicitly resolves the composition of individual aerosol particles and cloud droplets in a given population. Since individual particles and droplets are explicitly tracked, there

is no need to invoke ad hoc aging criteria that move aerosol mass between bins or modes as is the case with traditional modal or sectional approaches (Riemer et al., 2003; Stier et al., 2005; Bauer et al., 2008; Jacobson, 2001). This modeling approach is therefore well-suited to simulate aerosol mixing state and investigate its impacts on climate-relevant aerosol properties.

The model was described in Ching et al. (2012) and Ching et al. (2016) and had been used to simulate the mixing state evolution of black-carbon-containing aerosol in the cloud-free atmosphere, followed by a process analysis to what extent the aged aerosol is able to undergo nucleation-scavenging as the particles compete for water vapor in an updraft. However, these studies did not include the effects of aqueous-phase chemistry ocurring within the cloud droplets. This is the motivation for this study, where we extended our modeling framework to include aqueous-phase chemistry within the cloud droplets that are forming on a divers population of particles, common to urban environments.

We focus on the following questions: (1) To what extent does cloud processing change the aerosol mixing state of the population that entered the cloud? (2) How does this change the cloud condensation number concentration? (3) What is the role of coagulation between the interstitial particles and cloud droplets for mixing state of the aerosol?

Section 2 describes the model components, the scenario setup, and the mixing state metrics used in this study. Section 3 presents the analysis of the simulation results. Section 4 summarizes our results.

2 Model description and metrics

2.1 Stochastic particle-resolved module PartMC-MOSAIC

Aerosol physical and chemical processes were simulated by the stochastic particle-resolved model PartMC-MOSAIC (Particle Monte Carlo-Model for Simulating Aerosol Interactions and Chemistry-Model for Simulating Aerosol Interactions and Chemistry, (Riemer et al., 2009; Zaveri et al., 2008)). The PartMC model simulates the evolution of per-particle composition of a large ensemble of computational particles in a well-mixed computational volume. In contrast to Lagrangian droplet models that have become popular in the cloud microphysics community (Shima et al., 2009; Grabowski et al., 2019), we did not track the position of particles and droplets within the computational volume.

The particle number concentration changes due to coagulation, emission and dilution, which are simulated by using a stochastic Monte Carlo sampling method (Riemer et al., 2009). Gas-phase chemistry and gas-particle partitioning are represented by the aerosol chemistry model MOSAIC, which includes CBM-Z for gas-phase photochemical reactions (Zaveri, 1999), MTEM for estimating mean activity coefficient of an electrolyte in a inorganic multicomponent solution (Zaveri, Easter, & Peters, 2005) and MESA for intraparticle solid-liquid partitioning for inorganic aerosols (Zaveri, Easter, & Wexler, 2005). The formation mechansim of secondary organic aerosol (SOA) in MOSAIC is based on SORGAM (Schell et al., 2001) with several parameters adjusted to bring the simulated values closer to observation (Zaveri et al., 2010). The model represents key aerosol species including sulfate, nitrate, ammonium, black carbon (BC), primary organic aerosol (POA) and several surrogate secondary organic aerosol (SOA) species. The coupled model PartMC-MOSAIC was applied in previous studies for simulating aerosol optical and CCN properties, black carbon aging time-scales and the black carbon absorption enhancement due to the coatings (Zaveri et al., 2010; Riemer et al., 2010; Fierce et al., 2017, 2020), focusing on mixing state evolution during cloud-free conditions. The model was also used for evaluating the impact of aerosol mixing state on cloud droplet formation (Ching et al., 2012, 2016), which will be explained in more detail in the next section.

2.2 Cloud parcel model and aqueous-phase chemistry

Ching et al. (2012) described the details of the particle-resolved cloud parcel model, which simulates a population of aerosol particles that experience cooling at a prescribed cooling rate and subsequent growth due to the condensation of water vapor. The condensational growth of the particles is calculated following Seinfeld et al. (2016). The driving force of the growth is the difference between droplet equilibrium saturation vapor pressure and the ambient vapor pressure of the environment. The equilibrium saturation vapor pressure is calculated by Köhler theory, and the particle hygroscopicity is determined using the parameterization of aerosol hygroscopicity developed by Petters and Kreidenweis (2007). We currently do not represent any entrainment of cloud-free air into the cloud, surface tension effects on droplet growth (Mayol-Bracero et al., 2002), or the loss of droplets from the air parcel owing to sedimentation.

The aim of this paper is to investigate impacts of in-cloud aqueous-phase chemistry on aerosol mixing state. To this end, we coupled the reduced Chemical Aqueous Phase Radical Mechanism (CAPRAM) 2.4 to PartMC-MOSAIC. The reduced CAPRAM model includes 183 reactions (including Henry's Law partitioning, dissociation reactions, photolysis reactions and other aqueous-phase reactions) and 113 species (Herrmann et al., 1999; Ervens, 2003). The mechanism treats the reactions of common radicals and radical anions, transition metal ions and organics with less than two carbon atoms. The CAPRAM mechanism was compared with measurements from the FEBUKO field campaign and Tilgner et al. (2005), and Wolke et al. (2005) showed that the simulation results can reproduce the observational data well. While the aqueous-phase chemistry involving transition metal ions and organic species is of great interest (Harris et al., 2013; Alexander et al., 2009; Lian et al., 2019; McNeill, 2015; Smith et al., 2014), our scope for this initial study is the in-cloud production of sulfate. A subset of the most relevant Henry's law, aqueous equilibria and chemistry reactions are summarised in Table 1.

Table 1. Kinetic data for a subset of CAPRAM 2.4 reactions

Henry's Law	Reaction	K_{298} (M atm^{-1})	$\Delta H/R$ (K)
R1	$NH_{3(g)} \longrightarrow NH_{3(aq)}$	60.7	3920
R2	$H_2O_{2(g)} \longrightarrow H_2O_{2(aq)}$	1.02×10^{5}	6340
R3	$O_{3(g)} \longrightarrow O_{3(aq)}$	1.14×10^{-2}	2300
R4	$NO_{2(g)} \longrightarrow NO_{2(aq)}$	1.2×10^{-2}	1263
R5	$SO_{2(g)} \longrightarrow SO_{2(aq)}$	1.24	3247
Aqueous equilibria	**Reaction**	K_{298}^{forward} (M^{-n} s^{-1})	$\Delta H/R$ (K)
R6	$SO_{2(aq)} + H_2O \rightleftharpoons HSO_3^- + H^+$	3.13×10^{-4}	1940
R7	$HSO_3^- \rightleftharpoons SO_3^{2-} + H^+$	6.22×10^{-8}	1960
R8	$HNO_{3(g)} \rightleftharpoons NO_3^- + H^+$	4.62×10^{6}	10500
R9	$NO_{2(aq)} + HO_{2(aq)} \rightleftharpoons HNO_{4(aq)}$	2.2×10^{9}	4.6×10^{-3}
R10	$NH_{3(aq)} + H_2O \rightleftharpoons NH_4^+ + OH^-$	3.17×10^{-7}	−560
Aqueous chemistry	**Reaction**	K_{298} (M^{-n} s^{-1})	$\Delta H/R$ (K)
R11	$HSO_3^- + O_{3(aq)} \longrightarrow SO_4^{2-} + H^+ + O_{2(aq)}$	3.7×10^{5}	−5530
R12	$SO_3^{2-} + O_{3(aq)} \longrightarrow SO_4^{2-} + O_{2(aq)}$	1.5×10^{9}	−5280
R13	$HSO_3^- + H_2O_{2(aq)} + H^+ \longrightarrow SO_4^{2-} + 2\,H^+ + H_2O$	7.2×10^{7}	−4000
R14	$H_2O_{2(aq)} + OH_{(aq)} \longrightarrow aHO_2 + H_2O$	3.0×10^{7}	−1680
R15	$HNO_{4(aq)} + HSO_3^- \longrightarrow HSO_4^- + H^+ + NO_3^-$	3.3×10^{5}	0

The original gas-phase chemistry mechanism Regional Atmospheric Chemistry Modeling (RACM) used in CAPRAM 2.4 was replaced with CBM-Z, which is the gas-phase mechanism native to PartMC-MOSAIC. In the current setting, aqueous chemistry, and the evaporation and condensation of gases (other than water vapor) to aqueous particles are enabled for particles with liquid water mass larger than 5×10^{-16} kg, which corresponds to solution droplets of 1 μm in diameter.

We used the CVODE (Cohen et al., 1996) solver of the SUNDIALS (Hindmarsh et al., 2005) package to solve the mass transfer and aqueous chemistry of the CAPRAM 2.4 reduced mechanism with the Backward Differentiation Formulas (BDF) and Newton Iteration, which is suitable for mathematically stiff systems, such as those treating multi-phase chemistry. To reduce the stiffness of the system, the Henry's Law partitioning of the strong acids H_2SO_4, HCl, and HNO_3 were combined with their first acid dissociation step.

2.3 The scenario settings

The scenario setting of this work followed the two-step method used in Ching et al. (2012). Step 1 represented the simulation of an "urban plume scenario" in a subsaturated environment using PartMC-MOSAIC. The purpose of this step was to produce simulated aerosol populations that cover a wide range of mixing states. These were then used in step 2 as inputs for particle-resolved cloud parcel simulations.

The urban plume case environment shown here was adopted from Zaveri et al. (2010), following a Lagrangian box modeling approach, where we assumed that the air parcel containing background air moved over a polluted urban environment. The initial condition of the aerosol consisted of two lognormal modes, with the number concentration, geometric mean diameter, standard deviation and composition for each mode as listed in Table 2. We used 10,000 computational particles to resolve the initial aerosol. Note that the number of computational particles changed over the course of the simulation depending on coagulation, particle emissions, and dilution with the background, but was kept between half and double the initial number of computational particles using doubling and halving procedures as described in Riemer et al. (2009).

Gas-phase initial conditions were set to 50 pbb ozone and low levels of other trace gases. The plume was diluted with background air at a rate of 1.5×10^{-5} s^{-1} that contained the same gas mixing ratios and aerosol concentrations as the initial condition. The simulation started at 6AM local time and lasted for 24 h with gas and aerosol emission entering the simulation during the first 12 h. We use the term "plume time", t_u, to refer to the elapsed time during this 24-h simulation in cloud-free conditions. The temperature was prescribed as shown in Figure 1. For simplicity we assumed that the temperature remained constant after the first 6 h. This is consistent with the air parcel staying in the fully mature mixed layer until sunset and in the residual layer thereafter. The resulting relative humidity varied between 52% and 95%, assuming that the total water content in the air parcel was constant.

The aerosol emission sources and their compositions are also listed in Table 2. The full state, including gas-phase mixing ratios and composition of all computational particles, was saved hourly to be used as input for the cloud parcel simulations in step 2. The mixing state of the aerosol in this simulation evolved because primary aerosol emissions aged owing to formation of secondary aerosol and to coagulation processes, while fresh emissions continued to enter during the first 12 hours of simulation. Overall, this scenario mimicked the evolution of an air parcel in a polluted urban area, and we summarized the results, including the mixing state evolution, in Section 3.1.

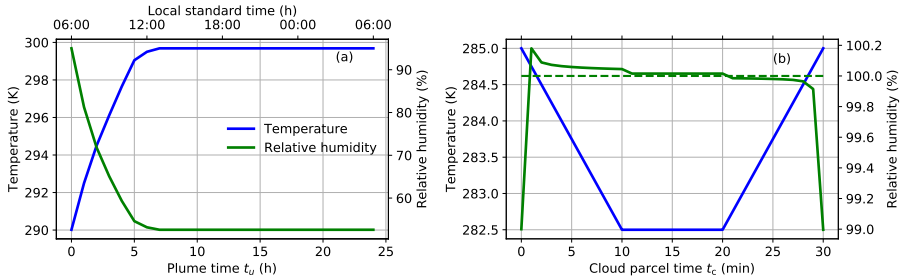

Figure 1. Temperature and relativity humidity time series in (a) urban plume environment and (b) cloud parcel environment. The green dashed line in (b) is RH = 100%.

Table 2. Size distributions and compositions of the initial, background and emitted aerosols

Initial/Background	N (cm^{-3})	D_g (μm)	σ_g	Composition by mass	D_i
Aitken mode	1800	0.02	1.45	49.6% $(NH_4)_2SO_4$ + 49.6% API1 + 0.8% BC	2.08
Accumulation mode	1500	0.116	1.65	49.6% $(NH_4)_2SO_4$ + 49.6% API1 + 0.8% BC	2.08
Emission	E ($m^{-2}s^{-1}$)	D_g (μm)	σ_g	Composition by mass	D_i
Cooking	9×10^6	0.086	1.91	100% POA	1
Diesel	1.6×10^8	0.05	1.74	70% BC + 30% POA	1.84
Gasoline	5×10^7	0.05	1.74	20% BC + 80% POA	1.65

For step 2, the hourly output of the simulated aerosol and gas-phase mixing ratios were used as input for the cloud parcel simulations, using a prescribed cooling rate. The temperature decreased for the first 10 minutes at a rate of 0.25 K/min. It was kept constant for the next 10 minutes, and increased at the rate of 0.25 K/min for the last 10 minutes. Hence one cloud cycle consisted of a total of 30 minutes, and we referred to the elapsed time within the cloud cycle as "cloud parcel time", t_c. The initial RH for the cloud parcel was 99 % and it reached supersaturation within less than 1 min. The parcel became subsaturated when the cloud began to evaporate at 20 minutes, and returned to RH=99% at the end of the simulation.

Since it is common for air parcels to undergo several cloud cycles (Barth et al., 2003), we conducted a total of four cloud cycles, which resulted in a total of $25\times4 = 100$ cloud parcel simulations. We initialized the aerosol of the second, third and fourth cloud cycle using the particle population from the end of the previous cloud cycle, and the gas-phase mixing ratios using the values from the beginning of the first cloud cycle. To explore the effects of coagulation, we performed the 100 cloud parcel cases without (base case) and with Brownian coagulation. For most of our analysis, we will focus on the difference between the particles at the start of the cloud parcel simulations ($t_c = 0$ min) and the end of the cloud parcel simulation (t_c = 30 min), after cloud evaporation.

2.4 Mixing state metrics

The objective of this paper is to quantify the change of particle mixing state as a result of cloud processing. The metrics used to quantify mixing state were developed by

Riemer and West (2013). The mixing state metric χ is calculated by:

$$\chi = \frac{D_\alpha - 1}{D_\gamma - 1} \tag{1}$$

where D_α is the average particle diversity and D_γ is the bulk particle diversity.

The calculation of these diversity metrics is based on the per-particle mixing entropy H_i. For an aerosol population of N particles containing A species, the mixing entropy H_i and particle diversity D_i of particle i are calculated as

$$H_i = \sum_{a=1}^{A} -p_i^a \ln p_i^a \quad D_i = e^{H_i} \tag{2}$$

where p_i^a is the mass fraction of species a in particle i. Expanding D_i to the whole population, D_α and D_γ are defined as

$$H_\alpha = \sum_{i=1}^{N} p_i H_i \qquad D_\alpha = e^{H_\alpha}, \tag{3}$$

$$H_\gamma = \sum_{a=1}^{A} -p_a H_i \qquad D_\gamma = e^{H_\gamma} \tag{4}$$

where p_i and p_a are the mass fractions of particle i and species a in the population. For externally mixed populations where particles contain only one species, $D_\alpha = 1$ and $\chi = 0\%$. For internally mixed population where each particle has the same composition as the bulk, $D_\alpha = D_\gamma$ and $\chi = 100\%$. In the ambient atmosphere, aerosols are neither completely internally nor externally mixed and intermediate mixing states are common (Healy et al., 2014; Ye et al., 2018; Ching et al., 2019). For regions close to emission sources, χ is expected to be lower, while χ is larger in air masses dominated by an aged aerosol.

The mixing state metrics χ defined in this paper used the abundance of model chemical species as the basis for calculating particle mass fractions in Equations (2)–(4), i.e. sulfate, nitrate, ammonium, POA, etc., excluding aerosol water. Other choices for defining "species" are possible, for example Ching et al. (2017) used two surrogate species, hygroscopic and non-hygroscopic species, as the basis for χ, and Zheng et al. (2021) compared χ based on the mixing of model chemical species, of hygroscopic and non-hygroscopic species, and of absorbing and non-absorbing species.

3 Simulation results

3.1 Urban plume simulation with PartMC-MOSAIC

This section summarizes the results from the urban plume simulation to provide context for the cloud parcel simulations discussed in the remainder of the paper. Figure 2 shows selected quantities from the urban plume simulation. The total particle number concentration N_a increased initially due to the emission of primary particles, reached a maximum of 15,295 cm^{-3} at $t_\mathrm{p} = 12$ h, then decreased because the emissions ceased, and both dilution and coagulation reduced the particle number concentration. Similarly, BC and POA mass concentrations increased for the first 12 h due to emission, and decreased thereafter due to dilution with the background, just as Figure 2b shows. The time series of the secondary aerosol species sulfate and SOA were determined by the interplay of loss by dilution and photochemical production. The ammonium nitrate mass concentration was determined by the gas concentrations of its precursors, HNO_3 and NH_3, temperature and RH. Mixing ratios of SO_2, O_3 and H_2O_2 are shown in Figure 2c for reference because they are directly involved in the in-cloud sulfate formation as discussed in Section 3.2.

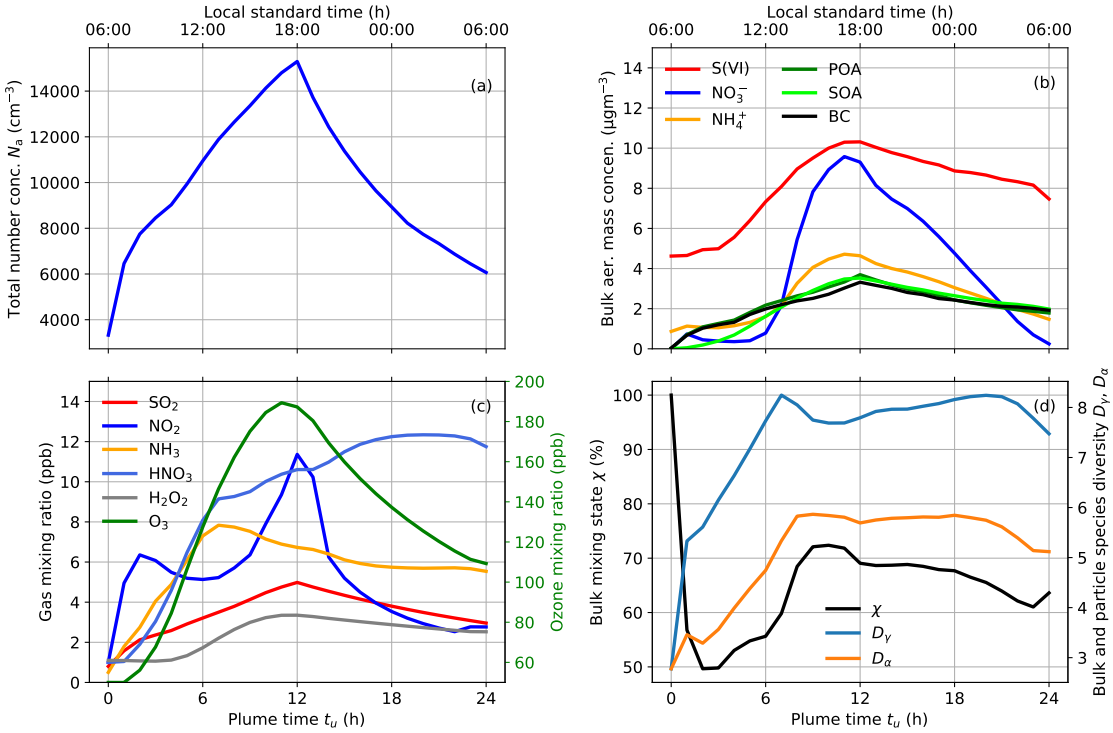

Figure 2. Temporal variation of (a) total number concentration, (b) mass concentrations of selected aerosol species, (c) mixing ratios of selected gas-phase species and (d) aerosol mixing state metrics.

Figure 2b only displays the bulk composition of the aerosol, while the mixing state information available from the particle-resolved output remains hidden. Figure 2d provides insight into the evolution of aerosol mixing state as quantified by the mixing state metrics introduced in Section 2.4. At $t_u = 0$, the particle population was completely internally mixed, and therefore the mixing state index χ was initially 100%.

From Equation 1, we recall that χ is determined by the ratio of D_α and D_γ. Figure 2d indicates that both D_α and D_γ started out low, which is consistent with the aerosol initially only containing a small number of species, both on a per-particle level and on a population level, see Table 2. Over the course of the simulation, both D_α and D_γ increased, but at different rates, which led to changes in χ that we can interpret as changes in mixing state. The initial decrease in χ to about 50% was caused by the emission of fresh combustion particles, containing BC and POA. These emissions continued for the first 12 h of simulation, but at the same time coagulation and secondary aerosol formation occurred, which (at least initially) efficiently increased the average per-particle diversity D_α. Overall, this led to a more internally mixed population, with χ increasing to 72% at 10 h. After this, dilution became relatively more important, introducing background particles, and ammonium nitrate evaporated almost entirely towards the end of the simulation. These combined processes resulted in a slow decrease in χ to 64% at the end of simulation.

3.2 Aerosol composition changes during cloud processing

As described in Section 3.1, for each hourly output from the urban plume simulation, four cloud cycles were simulated using the same temperature profile, shown in Figure 1b. In this section, we first illustrated the compositional changes during cloud processing, using the aerosol population from $t_u = 12$ h as the initial conditions for the cloud parcel simulation, and focus on the first cloud cycle ($N_{cycle} = 1$).

Figure 3a shows the evolution of several key variables for this case. The cloud parcel simulation started with RH=99%, and supersaturation and cloud droplet formation occurred after less than 1 min. During the first 10 min the liquid water content increased and reached a maximum of 1.23 $g\,kg^{-1}$ at 10 min. We determined the cloud droplet number concentration following the strategy used in Ching et al. (2012), where particles with wet diameter larger than 2 μm were classified as cloud droplets. As shown in the figure, the cloud droplet number concentration was 2011 cm^{-3} at the time when the maximum supersaturation was reached. This number concentration decreased somewhat as the relative humidity slowly relaxed to saturation, which can be explained by the so-called "inertial effect" (Chuang et al., 1997; Nenes et al., 2001). This refers to droplets with diameter larger than 2 μm that were not truly activated, i.e. they had a critical diameter larger than 2 μm and this critical diameter was not reached during the simulation time. After 20 min, as the RH dropped below 100%, the cloud droplet number concentration declined faster and the cloud evaporated.

Figure 3b and Figure 3c show the evolution of several key gas and aqueous-phase species. Ammonia in the gas-phase dissolved and immediately formed ammonium within the first minute. Aqueous-phase NH_4^+ increased from 4.7 to 9.8 $\mu g\ m^{-3}$. Nitrate increased rapidly from 9.3 to 37.4 $\mu g\ m^{-3}$ at the beginning due to the uptake of HNO_3. These processes are explained by the R1-R10 reactions in Table 1. After this, nitrate was further formed through reaction R15.

The dissolved sulfur dioxide formed SO_3^{2-} and HSO_3^-, and could be oxidized to sulfate by aqueous-phase H_2O_2 or O_3 through R11-R15. The sulfate aqueous formation rates are highly pH-dependent, and the H_2O_2 oxidation reaction R13 is dominant for pH lower than 5, while the O_3 pathway R12 becomes more important for pH higher than 6 (Seinfeld et al., 2016; Shao et al., 2019). For the cases shown here, the cloud droplets were acidic, and therefore the oxidation by H_2O_2 dominated. Sulfur dioxide in the gas-phase decreased from 4.98 to 1.94 ppb, and the S(VI), including SO_4^{2-} and HSO_4^-, increased from 5.16 to 20.23 $\mu g\ m^{-3}$ during the simulation period.

The evolution of the number size distributions based on wet diameter is illustrated in Figure 3c. At $t_c = 0$, the size distribution peaked at 0.3 μm. As discussed above, in less than 1 min, a subset of the particles activated to form cloud droplets and the particle size distribution evolved from initially unimodal to bimodal, with the first peak representing the interstitial (not activated) particles and the second peak representing the cloud droplets. The interstitial aerosol remained unchanged since this simulation did not include coagulation. We will investigate the impact of coagulation further in Section 3.4.

With increasing liquid water content and aqueous chemistry processes occurring, the cloud droplets continued to grow and the droplet mode peaked at 11 μm at 20 min. The simulated droplet sizes are comparable to the ones collected from cloud samples during the field campaign HI-SCALE (Fast et al., 2019), where the observed median cloud droplets size was between 13 and 20 μm. However, the observed median cloud droplet number concentration was approximately 80 cm^{-3}, which was one order of magnitude lower than in our simulated cases, consistent with a higher aerosol loading in our cases.

Next, we will turn to the changes in aerosol size distributions. To provide a summary of the 25 individual cloud parcel simulations, we show here the average over all 25 scenarios with the variability amongst cases indicated by the standard deviation (col-

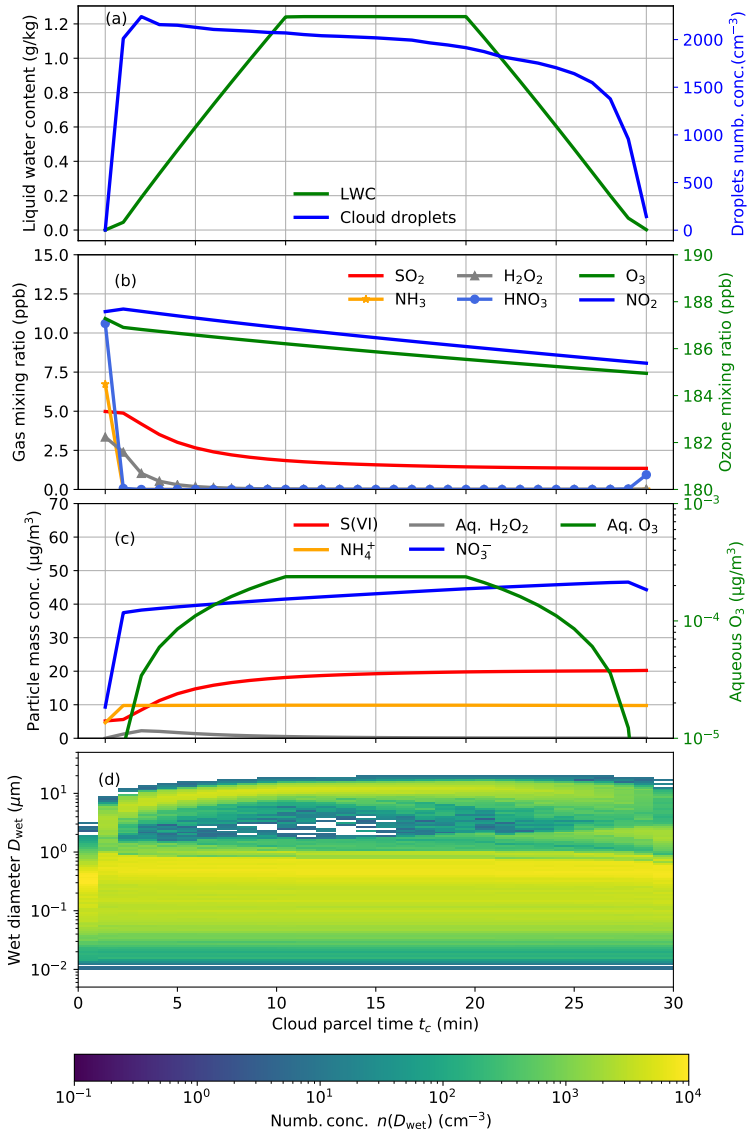

Figure 3. The evolution of (a) liquid water content (LWC) and cloud droplet number concentration (b) mixing ratios of key gas-phase species (c) key aqueous-phase species and (d) number concentration with respect to wet diameter. Results are for the aerosol population at $t_u = 12$ h and for $N_{cycle} = 1$.

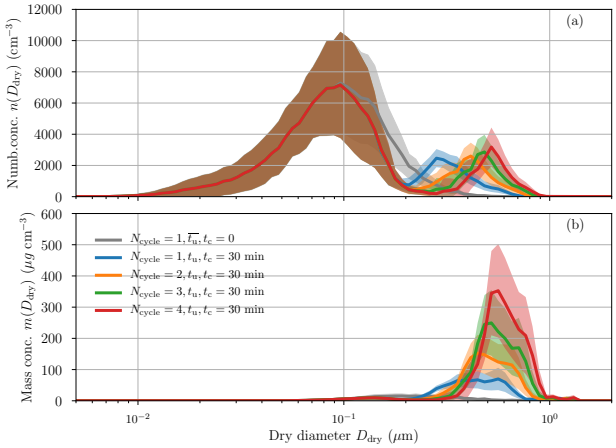

Figure 4. Change in (a) number and (b) mass size distribution with respect to dry diameter before the first cloud cycle and after each subsequent cloud cycle. The solid lines are the averaged distribution of all 25 plume cases in each cloud cycle. The shaded area represents the 1σ region of the 25 cases. The grey line is the distribution at $t_c = 0$ min, and the other lines are the distributions at the end of each cycle. Dry particles are evaluated at environment RH = 99%.

ored band). Figure 4 shows the number and mass concentration as a function of dry diameter before entering the cloud and after each cloud cycle. After the first cloud cycle, a second mode appeared for the dry number distribution, transforming the unimodal number distribution that peaked at a dry diameter of 0.1 μm to a bimodal distribution with a second peak at 0.3 μm. For each additional cloud cycle, the peak of the second mode kept moving to larger diameters and reached 0.5 μm after the fourth cloud cycle.

In order to quantify the diameter changes, we define the mean diameter $\bar{D}$ as

$$\bar{D} = \frac{\sum_{i=1}^{n} N_i D_i}{N_{\text{total}}}$$

where i is the particle index, n is the total number of computational particles, N_{total} is the total number concentration, N_i and D_i are the number concentration and diameter of computation particle i. The increase in diameter was largest for the first cycle, where $\bar{D}$ increased 24% and grew from 0.1 to 0.124 μm. The fourth cycle only led to a 5% mean diameter increase. For the mass, as shown in Figure 4b, distributions are dominated by the larger particles, as expected. Similar to the trend seen in the number size distribution, the mass increased most in the first cycle. Total dry mass of the particle population increased by 219% in the first cycle, while only by 38% in the last cycle.

Figure 5 shows the size-resolved mass fractions averaged over the 25 cases for each cloud simulation at the beginning of the first cloud cycle (grey) and at the end of the fourth cloud cycle (RH=99%). As expected, no change in the size-resolved composition occurred for particles smaller than about 0.1 μm, as these particles remained interstitial aerosol. For the activated particles, the sulfate mass fraction increased from 9.6% to 38.7% in the size range of 0.14–0.25 μm, and the nitrate mass fraction increased from 2.8% to 56.8% in the size range of 0.21–0.89 μm. Roth et al. (2016) also found that particles were more enriched with nitrate and sulfate after cloud processing from the samples collected in the HCCT-2010 field campaign. For the particles in size range of 0.1–0.2 μm, the fraction of inorganic and SOA species decreased and the fraction of POA

and BC species increased after cloud processing. This can be explained by the fact that there were two groups of particles in this size range, one group with mainly inorganic species and SOA, and the other group with mainly BC and POA. Particles in the first group were activated and grew larger due to cloud processing. Because more ammonium sulfate and nitrate was produced than SOA, the fraction of inorganics increased more than the SOA fraction. As a result, in the size range of 0.7–0.9 μm, particles transferred from organics-dominant to inorganics-dominant. Results showed that even in the same size ranges (here 0.1–0.2 μm), particles with different compositions can evolve differently. This is challenging to resolve for models that represent composition with one-dimensional distributions, assuming internally mixed particles within one size bin.

For our current work, the cloud simulations were set up using the temperature profile shown in Fig. 1b. Specifically, we considered a cloud that was maintained for about 30 min. In the real environment, clouds may last from minutes to days, depending on cloud type and the surrounding environment (Cotton et al., 2010), and they may also experience a range of different updraft velocities. Since the largest rate of secondary mass formation occured within a few minutes after the cloud formed, shortening the cloud parcel time did not impact the conclusions as long as the first few minutes were captured. With longer cloud lifetime, secondary aerosol mass formation may continue, provided that the reactants are not depleted. Variations in updraft velocities/cooling rates will result in different maximum supersaturations, and hence differences in the subpopulations of activated particles. We did not explore these sensitivities here to keep the scope focused on the changes of particle populations after typical but complete cloud processes.

The previous analyses showed the size-resolved state of the aerosol. However, even within a certain size range, particles can exhibit differences in composition, and we introduced this earlier as the aerosol mixing state. With our particle-resolved modeling approach, we are able to resolve this detail and quantify how aerosol mixing state changes with cloud processing. In order to visualize the change in aerosol mixing state, Figure 6 displays the two-dimensional size distribution of sulfate mass fraction $n(D_{\mathrm{dry}}, w_{\mathrm{SO_4}})$ for the example of two plume hours $t_{\mathrm{u}} = 0$ and $t_{\mathrm{u}} = 12$ h, before entering the cloud simulation and after four cloud cycles. At the beginning of the urban plume simulation ($t_{\mathrm{u}} =$ 0 min), all particles had the same composition, and $n(D_{\mathrm{dry}}, w_{\mathrm{SO_4}})$ was 36% across the entire population (Figure 6a). Over the course of the urban plume simulation, $n(D_{\mathrm{dry}}, w_{\mathrm{SO_4}})$ was controlled by condensation, coagulation and dilution processes, and it became more diverse as shown in Figure 6b. The aerosol primary emissions consisted of BC- and POA-containing particles (from gasoline, diesel and cooking emissions), which over time became coated with sulfate (as well as nitrate and SOA), resulting in particles with sulfate mass fraction of about 20% or less. In Figure 6b, particles in the size range of 0.01–0.2 μm appeared with a sulfate mass fraction of 70%. These are background particles that were introduced into the simulation by dilution with their initial SOA content (model species API1) having evaporated. The low particle number concentrations in between these main particle types originate from coagulation events.

Figure 6c and Figure 6d show the distributions after four cloud cycles. Note that the initial concentrations of the gas-phase species between the two plume hours differed as shown in Figure 2c. Using the population at $t_{\mathrm{u}} = 0$ h, all particles started with the same composition, and particles with diameters larger than 0.1 μm underwent cloud processing, resulting in sulfate mass fractions between 30 and 60%. Since we started with particles that were all identical and after cloud processing, the particles differ in sulfate mass fractions (and other secondary species), the aerosol population became more diverse and more externally mixed. Using the population at $t_{\mathrm{u}} = 12$ h, we can still see the signature of the particles that underwent cloud processing, however, it is difficult to infer if the population became more internally or externally mixed. This is where calculating mixing state metrics will help, which we will investigate next.

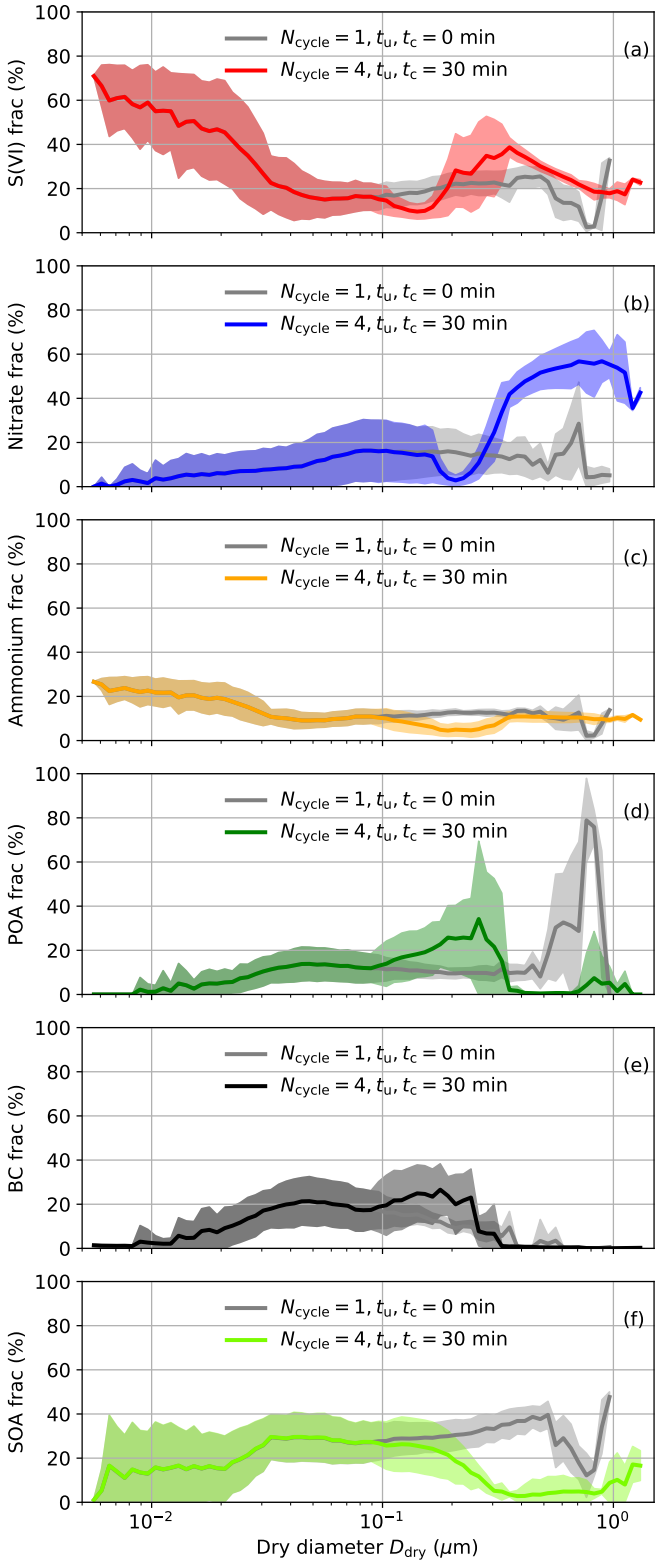

Figure 5. Size-resolved mass fractions of (a) S(VI), (b) nitrate, (c) ammonium, (d) POA, (e) BC and (f) SOA at $t_c = 0$ min of the first cloud cycle (grey lines), and $t_c = 30$ min after the fourth cloud cycle (colored lines). Solid lines are the average values of all 25 cases at each cycle and the shaded band represents the range of one standard deviation.

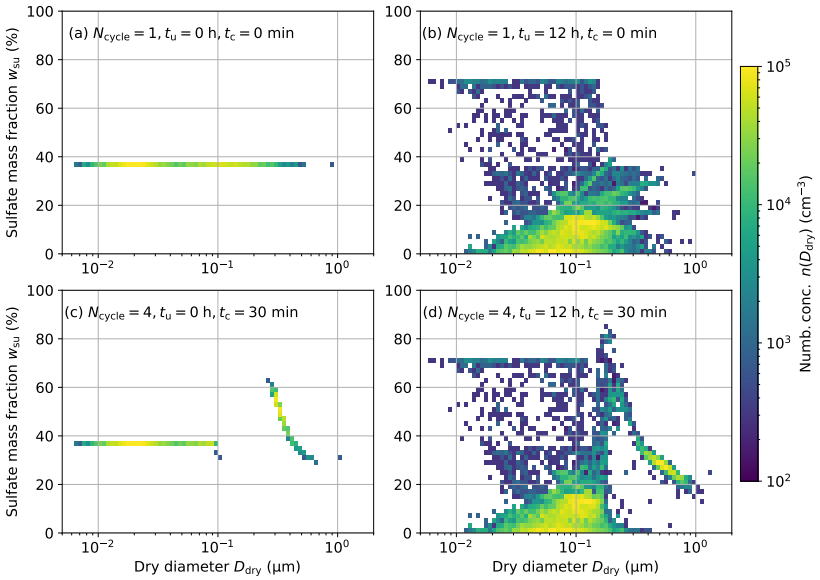

Figure 6. Two-dimensional number concentration distribution $n(D_p, w_{SO4})$ before cloud processing for (a) $t_u = 0$ h and (b) $t_u = 12$ h, (c) population from (a) after four cloud cycles, (d) population from (b) after four cloud cycles.

3.3 Impacts on mixing state and cloud condensation nuclei concentration

As shown qualitatively in Figure 6, cloud processes can change the diversity and the mixing state of particle populations. In this section we will quantify these changes for our cases more precisely using the metrics described in Section 2.4. Figure 7 shows the evolution of D_α, D_γ and χ after each of the four cloud cycles. After the first cloud cycle, the average particle species diversity D_α increased for aerosols that used plume hours 0 to 6 as inputs for the cloud parcel simulations. These populations started with relatively low average particle diversities. In contrast, D_α decreased for aerosols that used plume hours 7 to 24 as inputs for the cloud parcel simulations. This illustrates the fact that the addition of aerosol mass (mainly sulfate and nitrate) to a subset of particles in a population can lead to a decrease or increase in average particle diversity, depending on what the starting point is. When D_α was initially low, then adding secondary species led to more diverse particles, and D_α increased. This was the case when the aerosol consisted of different types of freshly emitted aerosol and the particles each only contained few species in the early stages of the urban plume simulation. When D_α was initially high, adding a small number of secondary species decreased the diversity, since those newly added species dominated. This was the case when the aerosol consisted of aged particles where several species commonly existed within one particle. This argument applies to both D_α and D_γ. Note that these two cases were contrasted in Riemer and West (2013) as "Prototypical cases 5 and 6". Comparing the different cloud cycles, we observed that each cloud cycle led to a less diverse population than the previous cloud cycle.

If D_α and D_γ changed at the same rate, then χ would remain unchanged by cloud processing. However, here D_α generally decreased less than D_γ, and therefore χ increased for each cloud parcel simulation. The freshly emitted particles experienced the largest

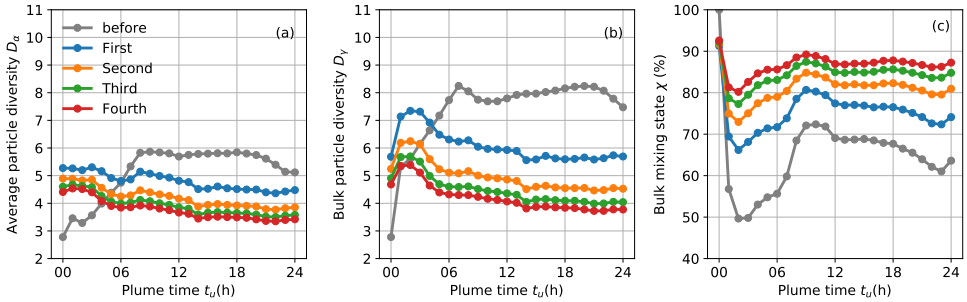

Figure 7. Evolution of average particle diversity D_α, bulk particle diversity D_γ and bulk mixing state χ (%) at the beginning of cloud cycle 1 and after each of the four cloud cycles. The black dashed line indicates $t_\mathrm{u} = 12$ h, which is used to graph the D_α-D_γ diagram in Figure 8.

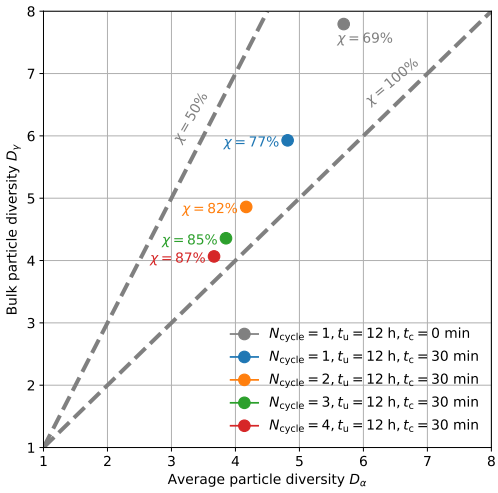

Figure 8. Average particle diversity D_α and bulk particle diversity D_γ diagram for the aerosol at $t_\mathrm{u} = 12$ h at the beginning of cloud cycle 1 and after each of the four cloud cycles.

changes, especially for urban plume particle populations at $t_\mathrm{u} = 2$ h, with χ increasing from 50% to 83% after four cycles. One exception was the case using the aerosol at $t_\mathrm{u} = 0$ h as input, which was 100% internally mixed. The first cloud cycle therefore led to a more external mixture (but subsequent cloud cycles led to more internal mixtures).

Figure 8 graphs the progression of the diversity metrics in a D_α- D_γ diagram using the aerosol at $t_\mathrm{u} = 12$ h as input as an example. After each cloud cycle, the mixing state index moved closer to the diagonal line which indicates a complete internal mixture ($\chi = 100\%$), with χ increasing from 69% to 87%. However, a complete internal mixture was never reached because the interstitial aerosol still contributed diversity.

CCN properties are determined by particle size and composition. As illustrated above, the activated particles grew during cloud processing and attained high hygroscopicity because of the added ammonium sulfate and ammonium nitrate. Particles with higher hygroscopicity and larger sizes have smaller critical supersaturation and activate at lower supersaturation level. Aerosol hygroscopicity has been observed to increase by 50% be-

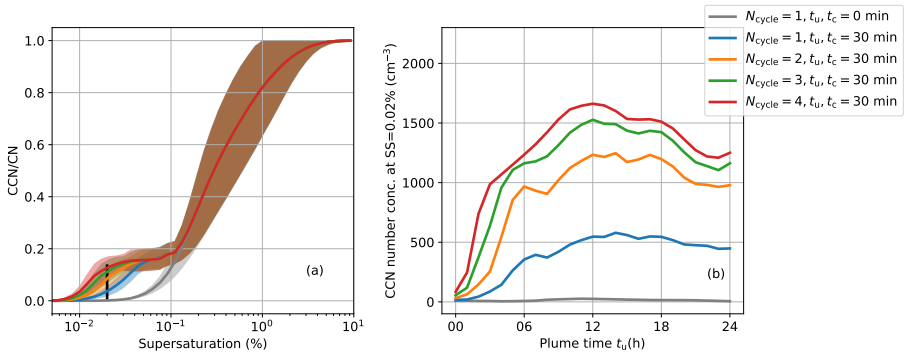

Figure 9. The change in (a) CCN spectrum and (b) CCN number concentration at ss = 0.02% after each of the four cloud cycles. Solid lines in (a) are the mean distributions of all 25 cases at each cycle and the shaded band represents the 1σ range. The black line in (a) indicates the supersaturation level at 0.02%

cause of the increased ammonium sulfate and ammonium nitrate mass fraction after cloud processing (Henning et al., 2014).

Figure 9a shows the change of CCN spectrum after each cloud cycle. As before, the solid lines indicate the average over the 25 urban plume cases and the shaded bands show the range of one standard deviation. For environmental supersaturations larger than 0.23%, the CCN/CN ratio remained unchanged after undergoing cloud processing. For supersaturations lower than 0.23%, the CCN/CN ratio increased with the largest increase occurring after the first cloud cycle. This is expected, since the interstitial aerosol remained unchanged during all cloud cycles, and only the particles that formed cloud droplets in the first cycle become progressively more easily activated (i.e. activate at lower and lower supersaturations).

Figure 9b illustrates the changes in CCN number concentration for the individual plume hours and an environmental supersaturation of 0.02%. Before cloud processing, the CCN number concentrations for all plume hours are less than 30 cm^{-3} at this supersaturation level. After cloud processing, the increase of CCN number concentration was significant, especially after the first cycle. For example, the population at $t_u = 12$ h experienced an increase of CCN concentration from 25 to 547 cm^{-3} after the first cycle, which corresponds to 2088%. The increase decreased with more cycles, and the increment is only 8.8% from cycle three to cycle four.

CCN concentrations for supersaturation thresholds larger than 0.23% did not change as a result of aqueous-phase chemistry. This particular threshold value was determined by the maximum supersaturation obtained in our cloud parcel simulations, which then governs the subpopulation of particles that activate. This threshold value is expected to increase for larger cooling rates which would result in larger maximum supersaturations (assuming the same aerosol population).

3.4 Effects of in-cloud coagulation on aerosol mixing state

So far we presented results that did not account for coagulation events within the cloud. We generally include two different coagulation mechanisms in PartMC, coagulation due to gravitational differential settling using the coagulation efficiencies according to Hall (1980), and Brownian coagulation (Jacobson, 2005). For the time scales, size ranges and number concentrations of droplets and interstitial aerosol particles in our cloud

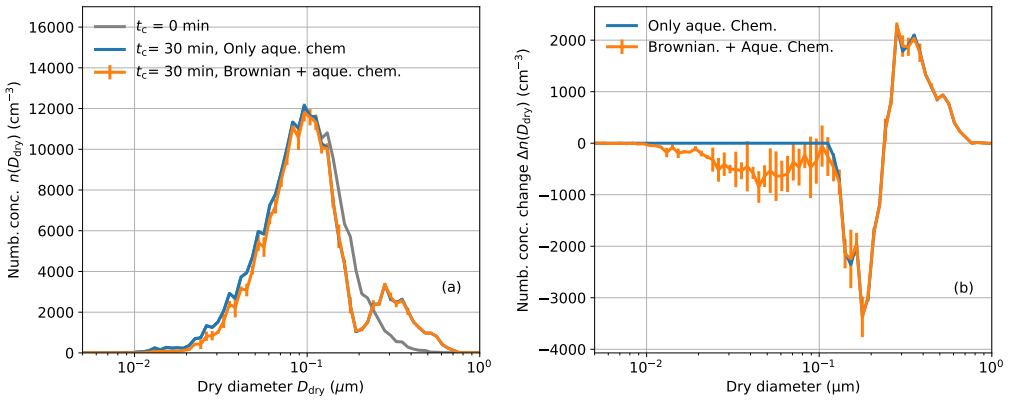

Figure 10. (a) Number distribution at initial condition $t_c = 0$ (grey), at $t_c = 30$ min with aqueous chemistry only (blue) and at $t_c = 30$ min with Brownian coagulation and aqueous chemistry (orange) (b) the change of number size distribution due to aqueous chemistry and Brownian coagulation. The solid orange line is the average of three realizations of the cloud parcel model simulation and the error bar is the 95% confidence interval.

parcel simulations, coagulation due to gravitational differential settling was negligible, and therefore we focus the discussion on the impact of Brownian coagulation, using the aerosol from $t_u = 12$ h as input. This population had the largest total number concentration (see Figure 2a), and so we expected the impacts of Brownian coagulation to be maximized for this case. Because coagulation events were simulated stochastically and introduce an element of randomness into our simulations, we repeated the cloud parcel simulation three times and report the average and 95% confidence interval.

Figure 10a compares the number distribution before and after the first cloud cycle including only aqueous chemistry and including aqueous chemistry and coagulation. For the case without Brownian coagulation, the size distribution did not change for diameters smaller than 0.1 μm. With Brownian coagulation, the number concentration of particles smaller than 0.1 μm decreased slightly. The changes in number size distributions comparing $t_c = 0$ min and 30 min are shown in Figure 10b. Brownian coagulation rates were higher for particle pairs with large diameter difference. Here, Brownian coagulation depleted the number concentration of particles between $0.01-0.1$ μm (the interstitial aerosol). The effects of aqueous-phase chemistry occurred at larger sizes and moved the particles from $0.1-0.3$ μm to $0.3-0.5$ μm.

Since Brownian coagulation in the cloud mainly affected interstitial particles, the changes to the CCN spectrum were expected to be small and should be mainly visible for higher supersaturation levels. As shown in Figure 11, the CCN spectrum moved left only for supersaturation level higher than 0.2%. For example, with Brownian coagulation, the CCN/CN ratio increased by 4.1% from 0.74 to 0.77 at ss=0.5 %. Figure 11b shows the change of CN (total aerosol number concentrations) and CCN concentration in the simulated 30 minutes. Including Brownian coagulation caused a decrease of total aerosol concentration (by 5.9%) and of CCN concentration (by 1.7%), but the decrease of total aerosol concentration was larger, which led to the reported increase in CCN/CN ratio.

Figure 11c shows the evolution of D_α and D_γ using output from every minute during the cloud parcel simulation. The trajectory of the case with Brownian coagulation was almost identical with the case without Brownian coagulation, indicating negligible

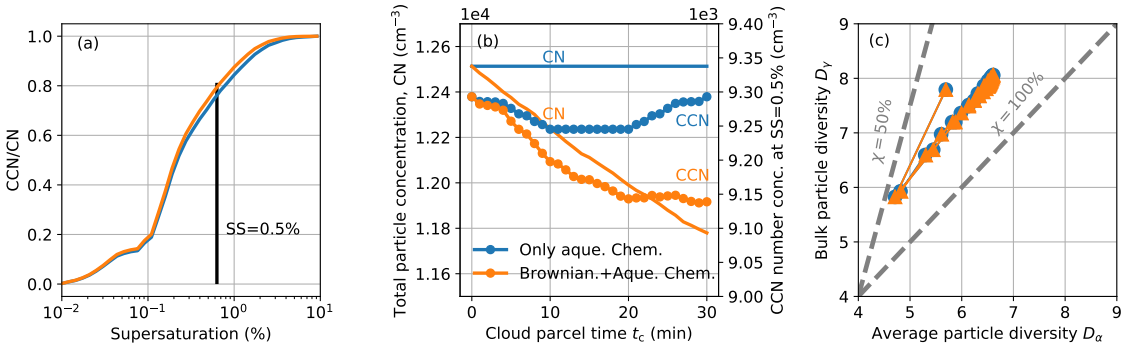

Figure 11. Changes in (a) CCN spectrum and (b) total CN and CCN concentration at ss = 0.5% with only aqueous chemistry only (blue) and with both Brownian coagulation and aqueous chemistry (orange). The vertical line in (a) is for ss = 0.5%, and solid and dotted lines in (b) are for total CN and CCN concentrations at that level respectively. (c) Effects of coagulation on aerosol mixing state metrics. The points correspond to output from every minute during the cloud parcel simulation.

effects of coagulation on mixing state. Although the differences were small, it was noticeable that including coagulation does not change D_γ, since the aerosol bulk mass concentrations were not changed. However, it increased D_α, since the average particle diversity increases during coagulation (archetypical Case 4 in Riemer and West (2013)).

4 Conclusions

In this study, we investigated the impact of in-cloud aqueous-phase chemistry on aerosol mixing state. Using the particle-resolved model PartMC-MOSAIC, we generated particle populations of different aerosol mixing states from an urban plume simulation representing polluted conditions. We used these as inputs for 30-min cloud parcel simulations that included the reduced CAPRAM 2.4 aqueous-phase chemistry mechanism. Each cloud parcel simulation was driven by the same temperature profile, with decreasing temperature during the first 10 min, constant temperature during the second 10 min, and increasing temperature during the third 10 min. While the cloud parcel simulations were simplified in that we assumed adiabatic conditions, our results were a first step towards investigating aerosol-cloud interactions within a particle-resolved framework that allows for representing aerosol mixing state without simplifying assumptions.

Coming back to the questions that we posed in the introduction, we concluded the following. We quantified changes in mixing state as a result of in-cloud processes using the diversity metrics D_α (average particle diversity) and D_γ (bulk aerosol diversity) and the mixing state index χ. The aqueous-phase chemistry processes had an "equalizing effect" on the diversity metrics, meaning that D_α and D_γ increased due to aqueous-phase chemistry when the initial values were low and decreased when the initial values were high. The first condition applied for plume time hours 0–6 in our scenario, when fresh emissions dominated which tend to be of low diversity, consistent with observational findings (Healy et al., 2014). Adding secondary species to the activated particles increased the diversities. The opposite was the case when D_α and D_γ values started out high, which applied to plume time hours 7–24, when the plume was aged. Here, adding secondary species to the activated particles decreased the diversities.

Whether the overall population became more or less internally mixed depended on the relative changes in D_α and D_γ. For most populations in our study, aqueous-phase chemistry led to a more internally mixed aerosol. For example, for the population of plume hour $t_u = 12$ h, χ increased from 69% to 77% after the first cloud cycle, and to 87% after the fourth cloud cycle. However, a completely internal mixture was not achieved under the conditions investigated here, since only a portion of the aerosol population activated and the remaining interstitial aerosol always contributed diversity to the population. An exception was the case of plume hour $t_u = 0$, when the initial aerosol population was completely internally mixed. In this case, aqueous-phase chemistry caused the population to become more externally mixed.

The size changes after cloud processing led to significant changes to aerosol microphysical properties. With ammonium nitrate and ammonium sulfate added to the activated particles, after the cloud evaporated, the activation potential of the resuspended aerosol particles increased remarkably for low supersaturation threshold. For example, the CCN concentration for particles from $t_u = 12$ h at supersaturation level 0.02% increased by a factor of 20 from 30 cm^{-3} to 547 cm^{-3} after the first cloud cycle. For subsequent cloud cycles, the increase was smaller and by the fourth cycle, it was only 8.8%.

The effects of coagulation due to gravitational settling were negligible in our simulations. This can be explained by the fact that the cloud droplets did not grow large enough for gravitational settling to take over as main coagulation mechanisms. Brownian coagulation occurred mainly between the interstitial particles at around 0.1 μm and cloud droplets at 10 μm. The number concentration reduction caused by coagulation was up to 5.8 % in the cases considered while the CCN concentration was reduced by less than 2%. This therefore resulted in an increase of the CCN/CN ratio for supersaturations higher than 0.2%. The change in aerosol mixing state caused by coagulation was negligible. It should be noted that our simulations did not take into account the impact of phoretic or turbulence effects on coagulation, which could modify the efficiency of in-cloud coagulation.

Acknowledgments

Yu Yao, Nicole Riemer and Matthew L. Dawson acknowledge funding from the National Science Foundation, Atmospheric and Geospace Sciences NSF AGS CAREER grant 1254428. This publication was also developed under Assistance Agreement no. EPA 83588101 awarded by the US Environmental Protection Agency to the Regents of the University of California. It has not been formally reviewed by the EPA. The views expressed in this document are solely those of the authors and do not necessarily reflect those of the agency. The EPA does not endorse any products or commercial services mentioned in this publication. The simulation data of particle-resolved modeling is available at `https://doi.org/10.13012/B2IDB-8367769_V1`.

References

Alexander, B., Park, R. J., Jacob, D. J., & Gong, S. (2009). Transition metal-catalyzed oxidation of atmospheric sulfur: Global implications for the sulfur budget. *Journal of Geophysical Research: Atmospheres*, *114*(2), 1–13. doi: https://doi.org/10.1029/2008JD010486

Andrejczuk, M., Reisner, J., Henson, B., Dubey, M., & Jeffry, C. (2008). The potential impacts of pollution on a nondrizzling stratus deck: Does aerosol number matter more than type? *Journal of Geophysical Research: Atmospheres*, *113*, D19204. doi: https://doi.org/10.1029/2007JD009445

Barth, M. C. (2006). The importance of cloud drop representation on cloud photochemistry. *Atmospheric Research*, *82*(1-2), 294–309. doi: https://doi.org/10.1016/j.atmosres.2005.10.008

Barth, M. C., Sillman, S., Hudman, R., Jacobson, M. Z., Kim, C. H., Monod, A., & Liang, J. (2003). Summary of the cloud chemistry modeling intercomparison: Photochemical box model simulation. *Journal of Geophysical Research: Atmospheres*, *108*(7). doi: https://doi.org/10.1029/2002jd002673

Bauer, S., Wright, D., Koch, D., Lewis, E., McGraw, R., Chang, L.-S., ... Ruedy, R. (2008). MATRIX (Multiconfiguration Aerosol TRacker of mIXing state): an aerosol microphysical module for global atmospheric models. *Atmospheric Chemistry and Physics*, *8*(20), 6003–6035. doi: https://doi.org/10.5194/acp-8-6003-2008

Bhattu, D., & Tripathi, S. N. (2015). CCN closure study: Effects of aerosol chemical composition andmixing state. *Journal of Geophysical Research: Atmospheres*, *120*(2), 766–783. doi: https://doi.org/10.1002/2014JD021978

Bondy, A. L., Bonanno, D., Moffet, R. C., Wang, B., Laskin, A., & Ault, A. P. (2018). The diverse chemical mixing state of aerosol particles in the southeastern United States. *Atmospheric Chemistry and Physics*, *18*(16), 12595–12612. doi: https://doi.org/10.5194/acp-18-12595-2018

Bott, A., Trautmann, T., & Zdunkowski, W. (1996). A numerical model of the cloud-topped planetary boundary layer: Radiation, turbulence and spectral microphysics in marine stratus. *Quarterly Journal of the Royal Meteorological Society*, *122*, 635–667. doi: https://doi.org/10.1002/qj.49712253105

Broekhuizen, K., Chang, R. Y., Leaitch, W. R., Li, S., & Abbatt, J. P. D. (2006). Closure between measured and modeled cloud condensation nuclei (CCN) using size-resolved aerosol compositions in downtown Toronto. *Atmospheric Chemistry and Physics*, *6*, 2513–2524. doi: https://doi.org/10.5194/acp-6-2513-2006

Ching, J., Adachi, K., Zaizen, Y., Igarashi, Y., & Kajino, M. (2019). Aerosol mixing state revealed by transmission electron microscopy pertaining to cloud formation and human airway deposition. *npj Clim Atmos Sci*, *2*(1), 22. doi: https://doi.org/10.1038/s41612-019-0081-9

Ching, J., Fast, J., West, M., & Riemer, N. (2017). Metrics to quantify the importance of mixing state for CCN activity. *Atmospheric Chemistry and Physics*, *17*, 7445-7458. doi: https://doi.org/10.5194/acp-17-7445-2017

Ching, J., & Kajino, M. (2018). Aerosol mixing state matters for particles deposition in human respiratory system. *SCIENTIFIC REPORTS*, *8*(1), 8864. doi: https://doi.org/10.1038/s41598-018-27156-z

Ching, J., Riemer, N., & West, M. (2012). Impacts of black carbon mixing state on black carbon nucleation scavenging: Insights from a particle-resolved model. *Journal of Geophysical Research: Atmospheres*, *117*(23), 1–21. doi: https://doi.org/10.1029/2012JD018269

Ching, J., Riemer, N., & West, M. (2016). Black carbon mixing state impacts on cloud microphysical properties: Effects of aerosol plume and environmental conditions. *Journal of Geophysical Research: Atmospheres*, 5990–6013. doi: https://doi.org/10.1002/2016JD024851

Chuang, P. Y., Charlson, R. J., & Seinfeld, J. H. (1997). Kinetic limitations on droplet formation in clouds. *Nature*, *390*(6660), 594–596. doi: https://doi.org/10.1038/37576

Cohen, S. D., Hindmarsh, A. C., & Dubois, P. F. (1996). CVODE, A Stiff/Nonstiff ODE Solver in C. *Computers in Physics*, *10*(2). doi: https://doi.org/doi:10.1063/1.4822377

Collett, J., Bator, A., Rao, X., & Demoz, B. B. (1994). Acidity variations across the cloud drop size spectrum and their influence on rates of atmospheric sulfate production. *Geophysical Research Letters*, *21*(22), 2393–2396. doi: https://doi.org/10.1029/94GL02480

Cooper, W., Bruintjes, R., & Mather, G. (1997). Calculations pertaining to hygroscopic seeding with flares. *Journal of Applied Meteorology*, *36*, 1449–1469.

Cotton, W. R., Bryan, G., & Van den Heever, S. C. (2010). *Storm and cloud dynamics*. Academic press.

Ervens, B. (2003). CAPRAM 2.4 (MODAC mechanism): An extended and condensed tropospheric aqueous phase mechanism and its application. *Journal of Geophysical Research: Atmospheres*, *108*(D14), 4426. doi: https://doi.org/10.1029/2002JD002202

Ervens, B. (2015). Modeling the processing of aerosol and trace Gases in clouds and fogs. *Chemical Reviews*, *115*(10), 4157–4198. doi: https://doi.org/10.1021/cr5005887

Fahey, K. M., Carlton, A. G., Pye, H. O., Baek, J., Hutzell, W. T., Stanier, C. O., ... Offenberg, J. H. (2017). A framework for expanding aqueous chemistry in the Community Multiscale Air Quality (CMAQ) model version 5.1. *Geoscientific Model Development*, *10*(4), 1587–1605. doi: https://doi.org/10.5194/gmd-10-1587-2017

Fast, J. D., Berg, L. K., Feng, Z., Mei, F., Newsom, R., Sakaguchi, K., & Xiao, H. (2019). The impact of variable land-atmosphere coupling on convective cloud populations observed during the 2016 HI-SCALE field campaign. *Journal of Advances in Modeling Earth Systems*, *11*(8), 2629–2654. doi: https://doi.org/10.1029/2019MS001727

Feingold, G., Kreidenweis, S. M., Stevens, B., & Cotton, W. (1996). Numerical simulations of stratocumulus processing of cloud condensation nuclei through collision coalescence. *Journal of Geophysical Research: Atmospheres*, *101*, 21391–21402. doi: https://doi.org/10.1016/0169-8095(94)90063-9

Fierce, L., Onasch, T. B., Cappa, C. D., Mazzoleni, C., China, S., Bhandari, J., ... Wolff, L. (2020). Radiative absorption enhancements by black carbon controlled by particle-to-particle heterogeneity in composition. *Proceedings of the National Academy of Sciences*, *117*(10), 5196–5203. doi: http://doi.org/10.1073/pnas.1919723117

Fierce, L., Riemer, N., & Bond, T. C. (2017). Toward reduced representation of mixing state for simulating aerosol effects on climate. *Bulletin of the American Meteorological Society*, *98*(5), 971–980. doi: http://doi.org/10.1175/BAMS-D-16-0028.1

Flossmann, A. (1994). A 2-D spectral model simulation of the scavenging of gaseous and particulate sulfate by warm marine clouds. *ATMOSPHERIC RESEARCH*, *32*, 233–248. doi: https://doi.org/10.1016/0169-8095(94)90063-9

Gao, W., Fan, J., Easter, R., Yang, Q., Zhao, C., & Ghan, S. J. (2016). Coupling spectral-bin cloud microphysics with the MOSAIC aerosol model in WRF-Chem: Methodology and results for marine stratocumulus clouds. *Journal of Advances in Modeling Earth Systems*, *8*, 1289–1309.

Grabowski, W. W., Morrison, H., Shima, S.-I., Abade, G. C., Dziekan, P., & Pawlowska, H. (2019). Modeling of cloud microphysics: Can we do better? *Bulletin of the American Meteorological Society*, *100*(4), 655–672. doi: https://doi.org/10.1175/BAMS-D-18-0005.1

Hall, D. W. (1980). A detailed microphysical model within a two-dimensional dynamic framework: model description and preliminary results. *Journal of the Atmospheric Sciences*, *37*, 2486-2507. doi: https://doi.org/10.1175/1520-0469(1980)037⟨2486:ADMMWA⟩2.0.CO;2

Harris, E., Sinha, B., Pinxteren, D. V., Tilgner, A., Fomba, K. W., Schneider, J., ... Herrmann, H. (2013). Enhanced role of transition metal oxidation of sO2. *Science*, *340*(6133), 727–730. doi: https://doi.org/10.1126/science.1230911

Healy, R., Riemer, N., Wenger, J., Murphy, M., West, M., Poulain, L., ... Evens, G. (2014). Single particle diversity and mixing state measurements. *Atmospheric Chemistry and Physics*, *14*, 6289-6299. doi: https://doi.org/10.5194/acp-14-6289-2014

Hegg, D. A., & Larson, T. V. (1990). The effects of microphysical parameterization on model predictions of sulfate production in clouds. *Tellus B*, *42*(3), 272–284. doi: https://doi.org/10.3402/tellusb.v42i3.15220

Henning, S., Dieckmann, K., Ignatius, K., Schäfer, M., Zedler, P., Harris, E., ... Stratmann, F. (2014). Influence of cloud processing on CCN activation behaviour in

the Thuringian Forest, Germany during HCCT-2010. *Atmospheric Chemistry and Physics*, *14*(15), 7859–7868. doi: https://doi.org/10.5194/acp-14-7859-2014

Herrmann, H., Ervens, B., Nowacki, P., Wolke, R., & Zellner, R. (1999). A chemical aqueous phase radical mechanism for tropospheric chemistry. *Chemosphere*, *38*(6), 1223–1232. doi: https://doi.org/10.1016/S0045-6535(98)00520-7

Hindmarsh, A. C., Brown, P. N., Grant, K. E., Lee, S. L., Serban, R., Shumaker, D. A. N. E., & Woodward, C. S. (2005). SUNDIALS : Suite of Nonlinear and Differential / Algebraic Equation Solvers. *ACM Transactions on Mathematical Software*, *31*(3), 363–396. doi: https://doi.org/10.1145/1089014.1089020

Hoag, K. J., Collett Jr, J. L., & Pandis, S. N. (1999). The influence of drop size-dependent fog chemistry on aerosol processing by san joaquin valley fogs. *Atmospheric Environment*, *33*(29), 4817–4832. doi: https://doi.org/10.1016/S1352-2310(99)00268-X

Hoose, C., Lohmann, U., Bennartz, R., Croft, B., & Lesins, G. (2008). Global simulations of aerosol processing in clouds. *Atmospheric Chemistry and Physics*, *8*(23), 6939–6963. doi: 10.5194/acp-8-6939-2008

Hoppel, W., Frick, G., & Larson, R. (1986). Effect of nonprecipitating clouds on the aerosol size distribution in the marine boundary layer. *Geophysical Research Letters*, *13*(2), 125–128. doi: https://doi.org/10.1029/GL013i002p00125

Jacobson, M. Z. (2001). Strong radiative heating due to the mixing state of black carbon in atmospheric aerosols. *Nature*, *409*(6821), 695–697. doi: https://doi.org/10.1038/35055518

Jacobson, M. Z. (2005). *Fundamentals of atmospheric modeling*. Cambridge University Press.

Jaruga, A., & Pawlowska, H. (2018). libcloudph++2.0: aqueoous-phase chemistry extension of the particle-based cloud microphysics scheme. *Geoscientific Model Development*, *11*, 3623–3645. doi: https://doi.org/10.5194/gmd-11-3623-2018

Knopf, D. A., Alpert, P. A., & Wang, B. (2018). The role of organic aerosol in atmospheric ice nucleation: A review. *ACS Earth Space Chem.*, *2*(3), 168–202. doi: https://doi.org/10.1021/acsearthspacechem.7b00120

Kreidenweis, S., Walcek, C., Feingold, G., Gong, W., Jacobson, M., Kim, C.-H., ... Seinfeld, J. (2003). Modification of aerosol mass and size distribution due to aqueous phase so2 oxidation in clouds: Comparisons of several models. *Journal of Geophysical Research: Atmospheres*, *108*, 8630. doi: https://doi.org/10.1029/2002JD002697

Lance, S., Barth, M., & Carlton, A. (2017). Multiphase chemistry: Experimental design for coordinated measurement and modeling studies of cloud processing at a mountaintop. *Bulletin of the American Meteorological Society*, *98*(7), ES163–ES167. doi: https://doi.org/10.1175/BAMS-D-17-0015.1

Lesins, G., Chylek, P., & Lohmann, U. (2002). A study of internal and external mixing scenarios and its effect on aerosol optical properties and direct radiative forcing. *Journal of Geophysical Research: Atmospheres*, *107*(D10), AAC 5-1-AAC 5-12. doi: https://doi.org/10.1029/2001JD000973

Li, W., Li, P., Sun, G., Zhou, S., Yuan, Q., & Wang, W. (2011). Cloud residues and interstitial aerosols from non-precipitating clouds over an industrial and urban area in northern China. *Atmospheric Environment*, *45*(15), 2488–2495. doi: https://doi.org/10.1016/j.atmosenv.2011.02.044

Lian, X., Ou, J., Zhang, G., Li, M., Tang, M., Zhou, Z., ... Chen, D. (2019). In-cloud formation of secondary species in iron-containing particles. *Atmospheric Chemistry and Physics*, *19*(2), 1195–1206. doi: https://doi.org/10.5194/acp-19-1195-2019

Mayol-Bracero, O. L., Guyon, P., Graham, B., Roberts, G., Andreae, M. O., Decesari, S., ... Artaxo, P. (2002). Water-soluble organic compounds in biomass burning aerosols over amazonia 2. apportionment of the chemical composition and importance of the polyacidic fraction. *Journal of Geophysical Research: Atmospheres*, *107*(D20), LBA 59-1-LBA 59-15. doi:

https://doi.org/10.1029/2001JD000522
McNeill, V. F. (2015). Aqueous organic chemistry in the atmosphere: Sources and chemical processing of organic aerosols. *Environmental Science and Technology*, *49*(3), 1237–1244. doi: https://doi.org/10.1021/es5043707
Nenes, A., Ghan, S., Abdul-Razzak, H., Chuang, P. Y., & Seinfeld, J. H. (2001). Kinetic limitations on cloud droplet formation and impact on cloud albedo. *Tellus B: Chemical and Physical Meteorology*, *53*(2), 133–149. doi: https://doi.org/10.3402/tellusb.v53i2.16569
Noble, S. R., & Hudson, J. G. (2019). Effects of continental clouds on surface Aitken and accumulation modes. *Journal of Geophysical Research: Atmospheres*, *124*(10), 5479–5502. doi: https://doi.org/10.1029/2019JD030297
Ovchinnikov, M., & Easter, R. (2010). Modeling aerosol growth by aqueous chemistry in a nonprecipitating cloud. *Journal of Geophysical Research: Atmospheres*, *115*, D14210. doi: https://doi.org/10.1029/2009JD012816
Petters, M. D., & Kreidenweis, S. M. (2007). A single parameter representation of hygroscopic growth and cloud condensation nucleus activity. *Atmospheric Chemistry and Physics*, *7*(8), 1961–1971. doi: https://doi.org/10.5194/acp-7-1961-2007
Pye, H. O., Nenes, A., Alexander, B., Ault, A. P., Barth, M. C., Clegg, S. L., ... others (2020). The acidity of atmospheric particles and clouds. *Atmospheric Chemistry and Physics*, *20*(8), 4809–4888. doi: https://doi.org/10.5194/acp-20-4809-2020
Riemer, N., Ault, A. P., West, M., Craig, R. L., & Curtis, J. H. (2019). Aerosol mixing state: measurements, modeling, and impacts. *Reviews of Geophysics*, *57*, 187-249. doi: https://doi.org/10.1029/2018RG000615
Riemer, N., Vogel, H., Vogel, B., & Fiedler, F. (2003). Modeling aerosols on the mesoscale-γ: Treatment of soot aerosol and its radiative effects. *Journal of Geophysical Research: Atmospheres*, *108*(D19). doi: https://doi.org/10.1029/2003JD003448
Riemer, N., & West, M. (2013). Quantifying aerosol mixing state with entropy and diversity measures. *Atmospheric Chemistry and Physics*, *13*(22), 11423–11439. doi: https://doi.org/10.5194/acp-13-11423-2013
Riemer, N., West, M., Zaveri, R., & Easter, R. (2010). Estimating black carbon aging time-scales with a particle-resolved aerosol model. *Journal of Aerosol Science*, *41*(1), 143–158. doi: https://doi.org/10.1016/j.jaerosci.2009.08.009
Riemer, N., West, M., Zaveri, R. A., & Easter, R. C. (2009). Simulating the evolution of soot mixing state with a particle-resolved aerosol model. *Journal of Geophysical Research: Atmospheres*, *114*(9), 1–22. doi: https://doi.org/10.1029/2008JD011073
Rissler, J., Nordin, E. Z., Eriksson, A. C., Nilsson, P. T., Frosch, M., Sporre, M. K., ... Swietlicki, E. (2014). Effective density and mixing state of aerosol particles in a near-traffic urban environment. *Environmental Science and Technology*, *48*(11), 6300–6308. doi: https://doi.org/10.1021/es5000353
Roth, A., Schneider, J., Klimach, T., Mertes, S., Van Pinxteren, D., Herrmann, H., & Borrmann, S. (2016). Aerosol properties, source identification, and cloud processing in orographic clouds measured by single particle mass spectrometry on a central European mountain site during HCCT-2010. *Atmospheric Chemistry and Physics*, *16*(2), 505–524. doi: https://doi.org/10.5194/acp-16-505-2016
Schell, B., Ackermann, I. J., Hass, H., Binkowski, F. S., & Ebel, A. (2001). Modeling the formation of secondary organic aerosol within a comprehensive air quality model system. *Journal of Geophysical Research: Atmospheres*, *106*(D22), 28275–28293. doi: https://doi.org/10.1029/2001JD000384
Seinfeld, J. H., Bretherton, C., Carslaw, K. S., Coe, H., DeMott, P. J., Dunlea, E. J., ... Wood, R. (2016). Improving our fundamental understanding of the role of aerosol-cloud interactions in the climate system. *Proceedings of the National Academy of Sciences*, *113*(21), 5781–5790. doi: https://doi.org/10.1073/pnas.1514043113
Shao, J., Chen, Q., Wang, Y., Lu, X., He, P., Sun, Y., ... Alexander, B. (2019). Heterogeneous sulfate aerosol formation mechanisms during wintertime chinese haze

events: air quality model assessment using observations of sulfate oxygen isotopes in beijing. *Atmospheric Chemistry and Physics*, *19*(9), 6107–6123. doi: 10.5194/acp-19-6107-2019

Shima, S., Kusano, K., Kawano, A., Sugiyama, T., & Kawahara, S. (2009). The super-droplet method for the numerical simulation of clouds and precipitation: a particle-based and probabilistic microphysics model coupled with a non-hydrostatic model. *Quarterly Journal of the Royal Meteorological Society: A journal of the atmospheric sciences, applied meteorology and physical oceanography*, *135*(642), 1307–1320. doi: https://doi.org/10.1002/qj.441

Smith, J. D., Sio, V., Yu, L., Zhang, Q., & Anastasio, C. (2014). Secondary organic aerosol production from aqueous reactions of atmospheric phenols with an organic triplet excited state. *Environmental Science and Technology*, *48*(2), 1049–1057. doi: https://doi.org/10.1021/es4045715

Sölch, I., & Kärcher, B. (2010). A large-eddy model for cirrus clouds with explicit aerosol and ice microphysics and lagrangian ice particle tracking. *Quarterly Journal of the Royal Meteorological Society*, *136*(653), 2074–2093. doi: https://doi.org/10.1002/qj.689

Stier, P., Feichter, J., Kinne, S., Kloster, S., Vignati, E., Wilson, J., ... Petzold, A. (2005). The aerosol-climate model ECHAM5-HAM. *Atmospheric Chemistry and Physics*, *5*(4), 1125–1156. doi: https://doi.org/10.5194/acp-5-1125-2005

Tilgner, A., Majdik, Z., Sehili, A. M., Simmel, M., Wolke, R., & Herrmann, H. (2005). SPACCIM: Simulations of the multiphase chemistry occurring in the FEBUKO hill cap cloud experiments. *Atmospheric Environment*, *39*(23-24), 4389–4401. doi: https://doi.org/10.1016/j.atmosenv.2005.02.028

Unterstrasser, S., & Sölch, I. (2014). Optimisation of simulation particle number in a lagrangian ice microphysical model. *Geoscientific Model Development*, *7*, 695–709. doi: https://doi.org/10.5194/gmd-7-695-2014

Winkler, P. (1973). The growth of atmospheric aerosol particles as a function of the relative humidity—II. An improved concept of mixed nuclei. *JOURNAL OF AEROSOL SCIENCE*, *4*(5), 373–387. doi: https://doi.org/10.1016/0021-8502(73)90027-X

Wolke, R., Sehili, A. M., Simmel, M., Knoth, O., Tilgner, A., & Herrmann, H. (2005). SPACCIM: A parcel model with detailed microphysics and complex multiphase chemistry. *Atmospheric Environment*, *39*(23-24), 4375–4388. doi: https://doi.org/10.1016/j.atmosenv.2005.02.038

Ye, Q., Gu, P., Li, H. Z., Robinson, E. S., Lipsky, E., Kaltsonoudis, C., ... Donahue, N. M. (2018). Spatial variability of sources and mixing state of atmospheric particles in a metropolitan area. *ENVIRON SCI TECHNOL*, *52*, 6807-6815. doi: https://doi.org/10.1021/acs.est8b01011

Zaveri, R. A. (1999). A new lumped structure photochemical mechanism for large-scale applications. *Journal of Geophysical Research: Atmospheres*, *104*(D23), 30387–30415. doi: http://doi.org/10.1029/1999JD900876

Zaveri, R. A., Barnard, J. C., Easter, R. C., Riemer, N., & West, M. (2010). Particle-resolved simulation of aerosol size, composition, mixing state, and the associated optical and cloud condensation nuclei activation properties in an evolving urban plume. *Journal of Geophysical Research: Atmospheres*, *115*(17), 1–19. doi: https://doi.org/10.1029/2009JD013616

Zaveri, R. A., Easter, R. C., Fast, J. D., & Peters, L. K. (2008). Model for simulating aerosol interactions and chemistry (MOSAIC). *Journal of Geophysical Research: Atmospheres*, *113*(13), 1–29. doi: https://doi.org/10.1029/2007JD008782

Zaveri, R. A., Easter, R. C., & Peters, L. K. (2005). A computationally efficient Multicomponent Equilibrium Solver for Aerosols (MESA). *Journal of Geophysical Research: Atmospheres*, *110*(24), 1–22. doi: https://doi.org/10.1029/2004JD005618

Zaveri, R. A., Easter, R. C., & Wexler, A. S. (2005). A new method for multicomponent

activity coefficients of electrolytes in aqueous atmospheric aerosols. *Journal of Geophysical Research: Atmospheres*, *110*(2), 1–23. doi: http://doi.org/10.1029/2004JD004681

Zheng, Z., Curtis, J. H., Yao, Y., Gasparik, J. T., Anantharaj, V. G., Zhao, L., ... Riemer, N. (2021). Estimating submicron aerosol mixing state at the global scale with machine learning and earth system modeling. *Earth and Space Science*, *8*(2). doi: https://doi.org/10.1029/2020ea001500